



Generating quantum multicriticality in topological insulators by periodic driving

Paolo Molignini ^{1,*}, Wei Chen ^{1,2} and R. Chitra¹

¹*Institute for Theoretical Physics, ETH Zürich, 8093 Zurich, Switzerland*

²*Department of Physics, PUC-Rio, 22451-900 Rio de Janeiro, Brazil*



(Received 23 June 2019; accepted 6 March 2020; published 7 April 2020)

We demonstrate that the prototypical two-dimensional Chern insulator hosts exotic quantum multicriticality in the presence of an appropriate periodic driving: a linear Dirac-like transition coexists with a quadratic nodal looplike transition. This nodal loop gap closure is characterized by an enhanced chiral-mirror symmetry that is induced by the driving procedure. The existence of multiple universality classes can be unambiguously captured by extracting critical exponents and scaling laws with a single renormalization group approach based on the curvature function of the stroboscopic Floquet Hamiltonian. This procedure is effective regardless of whether the topological phase transitions are associated with anomalous edge modes or not. We comment on possible experimental realizations of the model and detection schemes for the curvature function.

DOI: [10.1103/PhysRevB.101.165106](https://doi.org/10.1103/PhysRevB.101.165106)

I. INTRODUCTION

Periodic driving provides an unprecedented channel to engineer exciting nonequilibrium quantum phases. Of particular interest are the various topological phases that can be achieved by periodic driving, such as Floquet topological insulators [1–6], Floquet topological superconductors [7–15], and various exotic Floquet semimetals [16–23], as well as nodal lines or loops [24]. Most importantly, this plethora of Floquet topological phases can be very efficiently tuned by simple manipulations of the drive. This versatility provides an unrivalled opportunity to investigate the quantum criticality near the topological phase transitions (TPTs).

In this paper, we demonstrate the feasibility of inducing TPTs belonging to multiple universality classes, as well as quantum multicriticality, by means of periodic driving in an otherwise ordinary, noninteracting topological insulator. This result is remarkable, given that in static systems with local Landau order parameters these features usually arise from the complicated interplay between various interacting and kinetic energy scales [25–29]. The identification of this unexpected multicriticality is based on a unified framework that views the topological order as a momentum space integration of a curvature function [30–34] and the generic feature that the curvature function and edge state decay length diverge [35] at the TPTs, from which the existence as well as coexistence of multiple universality classes and the scaling laws are uncovered.

To demonstrate the aforementioned features, we employ a prototypical two-dimensional (2D) Floquet-Chern insulator (FCI) that exhibits additional peculiar features that are themselves of extreme interest. First, this system hosts so-called anomalous phases—with no static counterpart—that break the ubiquitous bulk-edge correspondence: They are characterized

by a trivial stroboscopic bulk topology, while still exhibiting anomalous edge modes (AEMs) in the quasienergy spectrum [36–38]. We establish that anomalous TPTs can be well captured by stroboscopic physics and do not require knowledge of the full-time dependence (micromotion). Second, we uncover that an appropriate driving induces a *nodal loop semimetal* (NLS) due to an emergent chiral mirror symmetry, which corresponds to elusive topological nodal loop band inversions studied in the context of the spin Hall effect [39,40]. This suggests the feasibility of realizing exotic symmetry-induced topological states by choosing specific driving strategies. We will demonstrate that the unified scheme based on the momentum space curvature function allows the application of a curvature renormalization group (CRG) approach [30,31], which has been successfully applied to determine the phase boundaries in numerous interacting and noninteracting models, both static and periodically driven [14,30–34]. The CRG approach based on the stroboscopic Floquet Hamiltonian unambiguously captures the TPTs despite all the richness of multicriticality, AEMs, and emergent nodal loops.

II. MODEL AND TOPOLOGICAL DESCRIPTION

We consider a paradigmatic 2D FCI already realized in photonic lattices [36,37,41]. The model describes fermions with *modulated* nearest-neighbor hoppings on a square lattice:

$$\mathcal{H}(t) = \sum_{\mathbf{k}=(k_x, k_y)} \begin{pmatrix} c_{\mathbf{k},A}^\dagger & c_{\mathbf{k},B}^\dagger \end{pmatrix} H(\mathbf{k}, t) \begin{pmatrix} c_{\mathbf{k},A} \\ c_{\mathbf{k},B} \end{pmatrix},$$

$$H(\mathbf{k}, t) = - \sum_{n=1}^4 J_n(t) (e^{i\mathbf{b}_n \cdot \mathbf{k}} \sigma^+ + e^{-i\mathbf{b}_n \cdot \mathbf{k}} \sigma^-). \quad (1)$$

The lattice vectors $\mathbf{b}_1 = -\mathbf{b}_3 = (a, 0)$ and $\mathbf{b}_2 = -\mathbf{b}_4 = (0, a)$ connect the sublattices $\alpha = A, B$ on which the creation or annihilation operators $c_{\mathbf{k},\alpha}^{(\dagger)}$ act, and σ^\pm refer to Pauli matrices. A schematic illustration of the model is provided in Fig. 1. The hoppings $J_n(t)$ are periodically modulated with a four-step

*Present address: Clarendon Laboratory, University of Oxford, Oxford OX1 3PU, United Kingdom.

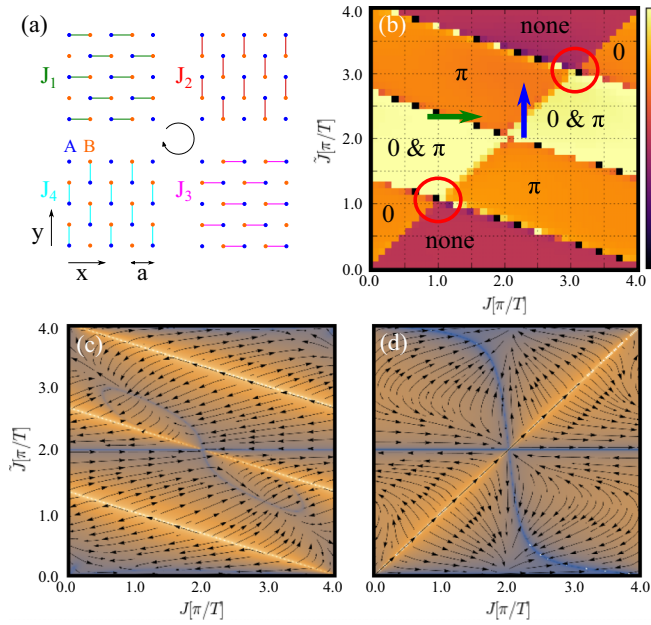


FIG. 1. (a) Depiction of the periodically driven 2D tight-binding model discussed in the main text. We consider a periodic four-step driving protocol for which the first hopping is different from the next three, $J \equiv J_1 \neq J_2 = J_3 = J_4 \equiv \tilde{J}$. (b) Phase diagram obtained from the time-integrated topological invariant, indicating the type of topological excitations in each phase. The arrows, also shown in Fig. 2, indicate the two classes of TPTs studied, while the red circles highlight multicritical points. (c), (d) CRG flow diagram evaluated at $\mathbf{k}_0 = (0, 0)$ and $\mathbf{k}_0 = (0, \pi)$ along direction $k_i = k_x$. The color codes indicate the log of the numerator of the CRG equation, $\log[\partial_{k_i}^2 F(\mathbf{k}_0, \mathbf{M})]$, with yellow being high values (critical lines) and blue low values (fixed lines). Choosing other HSPs [i.e., $(\pi, 0)$ and (π, π)] or the direction $k_i = k_y$, leads to similar flow diagrams.

protocol of period T , in which, during the n th step of the cycle, only the hopping J_n in direction \mathbf{b}_n is active [37]. Furthermore, we consider the special case of $J \equiv J_1 \neq J_2 = J_3 = J_4 \equiv \tilde{J}$ (see Fig. 1 for clarity). Note that this type of modulation inherently introduces a circular pattern of hoppings that enables the propagation of edge modes in a strip geometry [36,37]. As shown in Ref. [36], these modes are chiral and dispersive, whose group velocities are inversely proportional to the driving period.

We first briefly review how to construct topological invariants for 2D Floquet systems such as the FCI. For a general time-periodic system with open boundary conditions described by the Hamiltonian $H(t) = H(t + T)$, the full dynamics of the topological edge states is governed by the time evolution operator, defined as

$$U(t, 0) = \mathcal{T} \left\{ \exp \left[-i \int_0^t dt' H(t') \right] \right\}, \quad (2)$$

where \mathcal{T} is the time-ordering operator and we have set the initial time $t_0 = 0$ and $\hbar = 1$. The operator $U(t, 0)$ accounts for the full time dynamics, including the micromotion between periods. When $t \rightarrow T$, the time evolution operator is typically called a Floquet operator and, because of the underlying time periodicity, it fulfills $U(T, 0) = U(Tm, T(m-1))$ with

$m \in \mathbb{N}$. This induces a discrete quantum map that describes stroboscopic dynamics [42]. We can then define an effective stroboscopic Floquet Hamiltonian h_{eff} via $U(T, 0) \equiv e^{-ih_{\text{eff}}T}$. The effective stroboscopic Floquet Hamiltonian contains the full information about the system at multiples of the driving period T . Diagonalization of $h_{\text{eff}}T$ will then yield the stroboscopic quasienergy spectrum $\epsilon_{\alpha, k}$ of the Floquet-state solutions $\Psi_{\alpha}(k, t) = \exp(-i\epsilon_{\alpha, k}t)\Phi_{\alpha}(k, t)$, where $\Phi_{\alpha}(k, t) = \Phi_{\alpha}(k, t + T)$ [42]. Because of the T periodicity of the Floquet modes $\Phi_{\alpha}(k, t)$, the quasienergies are defined modulo $\frac{2\pi}{T} = \omega$. Therefore, we can restrict ourselves to consider a first ‘‘Floquet-Brillouin zone’’ of quasienergies $\epsilon_{\alpha} \in (-\omega/2, \omega/2)$. The number of stroboscopic edge modes can be determined as a function of the driving parameters from an analysis of the quasienergy spectrum, i.e., from gap closures and localization of 0 and π -quasienergy states. Consequently, the topological phase diagram of the stroboscopic system can be ascertained.

In analogy with time-independent systems, the number of edge modes in an open geometry is related to the properties of the bulk time evolution operator via a bulk-edge correspondence [36]. We could therefore determine the topological phase diagram by investigating the bulk time operator:

$$U_{\mathbf{k}}(t, 0) = \mathcal{T} \left\{ \exp \left[-i \int_0^t dt' H(\mathbf{k}, t') \right] \right\}. \quad (3)$$

In Ref. [36], it was shown that stroboscopic dynamics is in general insufficient to determine the correct number of edge modes generated in 2D systems like the one considered here. Micromotion, i.e., time evolution within a period, should be considered explicitly, and in general plays a crucial role in the definition and determination of the correct topological invariants [43,44]. In this case, the number of edge modes at quasienergy ϵ can be calculated from a topological invariant defined as the winding number of an explicitly time-dependent map $S^1 \times S^1 \times S^1 \rightarrow U(N)$ constructed from the bulk-time operator [36,45] $W[U_{\epsilon}] = \frac{1}{16\pi^2} \int dt dk_x dk_y \text{Tr} [U_{\mathbf{k}, \epsilon}^{-1} \partial_t U_{\mathbf{k}, \epsilon} [U_{\mathbf{k}, \epsilon}^{-1} \partial_{k_x} U_{\mathbf{k}, \epsilon}, U_{\mathbf{k}, \epsilon}^{-1} \partial_{k_y} U_{\mathbf{k}, \epsilon}]]$. Here, $U_{\mathbf{k}, \epsilon}(t, 0)$ is an operator derived from $U_{\mathbf{k}}(t, 0)$ preserving the number of edge modes at ϵ while smoothing the operator at the end of the cycle to the identity, i.e., $U_{\mathbf{k}, \epsilon}(T, 0) = \mathbb{1}$ [36]. This transformation is necessary because the winding number is equal to the number of edge modes at ϵ only if the spectrum of the bulk operator is gapped everywhere except at ϵ , which can be achieved only if $U_{\mathbf{k}, \epsilon}(T, 0) = \mathbb{1}$.

While the time-integrated topological invariant yields the correct number of edge modes, it is computationally quite cumbersome because of the triple integration and the additional manipulations performed on the time-evolution operator. Furthermore, if one is interested mainly in the criticality of the TPTs, such information should already be determined by the gap closures in the quasienergy spectrum at zero and π quasienergies, which can be readily extracted from the stroboscopic bulk effective Hamiltonian $h_{\text{eff}}(\mathbf{k})$ [14]. For a general unitary 2×2 -Floquet operator,

$$U_{\mathbf{k}}(T, 0) = \begin{pmatrix} A(\mathbf{k}) & B(\mathbf{k}) \\ -B(\mathbf{k})^* & A(\mathbf{k})^* \end{pmatrix}, \quad (4)$$

the effective Floquet Hamiltonian defined via $U_{\mathbf{k}}(T, 0) = e^{-ih_{\text{eff}}(\mathbf{k})T}$ takes the following form [14]:

$$h_{\text{eff}}(\mathbf{k}) \propto \text{Im}[B]\sigma^x + \text{Re}[B]\sigma^y + \text{Im}[A]\sigma^z \equiv \mathbf{n}(\mathbf{k}) \cdot \boldsymbol{\sigma}. \quad (5)$$

The quasienergy dispersions of the Floquet bands rescaled to $[-\pi, \pi)$ are then obtained as the eigenvalues of the operator $h_{\text{eff}}(\mathbf{k})T$. The topology of the stroboscopic bulk effective Hamiltonian is mapped by the Chern number [46], which for the two-band system analyzed here is $\mathcal{C} = -\frac{1}{2\pi} \int_{-\pi}^{\pi} dk_x \int_{-\pi}^{\pi} dk_y F(\mathbf{k})$, where

$$F(\mathbf{k}) = \hat{\mathbf{n}}(\mathbf{k}) \cdot [\partial_{k_x} \hat{\mathbf{n}}(\mathbf{k}) \times \partial_{k_y} \hat{\mathbf{n}}(\mathbf{k})] \quad (6)$$

is the Berry curvature of the Floquet band in question.

The Chern number \mathcal{C} of the effective bulk Hamiltonian counts the difference between the numbers of edge modes above and below each Floquet band [36]. If edge modes exist only at quasienergy 0 or $\pm\pi$, \mathcal{C} of each band will correctly capture the number of edge modes. However, for coexisting 0 and $\pm\pi$ modes $\mathcal{C} = 0$, the bulk-edge correspondence is broken, and we have a phase with AEMs [36]. The full phase diagram based on time-integrated topological invariants as defined in Ref. [36] is mapped in Fig. 1(b) as a function of the two hopping strengths J and \tilde{J} . We can distinguish multiple phases which are either topologically trivial, hosting only one edge mode at quasienergy 0 or π , or hosting AEMs. The topological phase boundaries have an analytical form given by $\tilde{J} = J$ and $\tilde{J} = \frac{1}{3}(n - J)$, where $n \in [1, 2, 3]$ [37].

III. DETECTION OF TPTs

Using the CRG method, we now show that information about the TPTs and their criticality can be extracted even in the presence of AEM from the stroboscopic Berry curvature alone, even though its integration \mathcal{C} is not necessarily equal to the true time-integrated topological invariant. We first briefly summarize the method developed originally for static systems in [30–33,47,48] and for Floquet systems in Ref. [14]. Generally, at any system parameters $\mathbf{M} = (J, \tilde{J})$, the curvature function peaks around high-symmetry points (HSPs) \mathbf{k}_0 satisfying $\mathbf{k}_0 = -\mathbf{k}_0$. Across the topological phase boundaries described by $\{\mathbf{M}_c\}$, the peaks diverge and flip signs to preserve the quantization of the Chern number [30,31,47]. The CRG relies on the scaling procedure $F(\mathbf{k}_0, \mathbf{M}') = F(\mathbf{k}_0 + \delta\mathbf{k}, \mathbf{M})$ that searches the trajectory in the parameter space along which the diverging peak $F(\mathbf{k}_0, \mathbf{M})$ is gradually flattened [30,31,47]. Defining $d\mathbf{l} \equiv \delta k^2$, $dM_i = M'_i - M_i$, the scaling procedure yields the renormalization group (RG) equation

$$\frac{dM_i}{d\mathbf{l}} = \frac{1}{2} \frac{\partial_{k_j}^2 F(\mathbf{k}, \mathbf{M})|_{\mathbf{k}=\mathbf{k}_0}}{\partial_{M_i} F(\mathbf{k}_0, \mathbf{M})}. \quad (7)$$

The topological phase diagram can be easily ascertained by analyzing the critical points of Eq. (7). Furthermore, the criticality of the TPT is characterized by the divergences of both $F(\mathbf{k}_0, \mathbf{M})$ and the concomitant inverse of the full width at half maximum in directions $i = x, y$ expressed as $\text{FWHM}_i \equiv \frac{2}{\xi_{k_{0,i}}}$, see also Refs. [30,31,34,47]. As $\mathbf{M} \rightarrow \mathbf{M}_c$, these quantities diverge like $F(\mathbf{k}_0, \mathbf{M}) \propto |\mathbf{M} - \mathbf{M}_c|^{-\gamma}$ and $\xi_{k_{0,i}} \propto |\mathbf{M} - \mathbf{M}_c|^{-\nu_i}$. The conservation of \mathcal{C} in a phase leads to

precise scaling laws relating γ and ν_i . For example, $\sum_i \nu_i = 1 + 1 = \gamma = 2$ for an isotropic 2D Dirac model [47].

The critical exponents obtained from the CRG analysis can be related to those assigned to correlation length and susceptibility in the Landau theory of phase transitions. For a 2D (stroboscopic) Hamiltonian described by (Floquet-)Bloch states $|u_{n\mathbf{k}}\rangle$, such as the one considered in this paper, we can write the Berry curvature as [49–51]

$$F(\mathbf{k}, \mathbf{M}) = \sum_{n \in v} \nabla_{\mathbf{k}} \times \langle u_{n\mathbf{k}} | i \nabla_{\mathbf{k}} | u_{n\mathbf{k}} \rangle \\ = -i \sum_{n \in v} \sum_{\mathbf{R}} e^{-i\mathbf{k} \cdot \mathbf{R}} \langle \mathbf{R}n | (\mathbf{R} \times \hat{\mathbf{r}})_z | 0n \rangle, \quad (8)$$

where $|\mathbf{R}n\rangle = \frac{1}{N} \sum_{\mathbf{k}} e^{i\mathbf{k} \cdot (\hat{\mathbf{r}} - \mathbf{R})} |u_{n\mathbf{k}}\rangle$ is the Wannier state centering at homecell \mathbf{R} , N denotes the number of lattice sites, and $\hat{\mathbf{r}}$ is the position operator. We emphasize that in our analysis of the Floquet problem we work with the Floquet bands derived from the *stroboscopic* effective Hamiltonian, and therefore the Wannier states calculated in this context are also to be interpreted as *stroboscopic* states. The Wannier representation allows us to draw a direct correspondence between the topological description of the system and the theory of orbital magnetization for 2D TRS-breaking systems [52–56]. In this picture, the Fourier transform of the curvature function yields a Wannier state correlation function,

$$\tilde{F}_{2D}(\mathbf{R}) = \frac{1}{(2\pi)^2} \iint d^2k e^{i\mathbf{k} \cdot \mathbf{R}} F(\mathbf{k}, \mathbf{M}) \\ = -i \sum_{n \in v} \langle \mathbf{R}n | (\mathbf{R} \times \mathbf{r})_z | 0n \rangle \\ = -i \sum_{n \in v} \int d^2r W_n^*(\mathbf{r} - \mathbf{R}) (\mathbf{R} \times \hat{\mathbf{r}}) W_n(\mathbf{r}) \\ \propto e^{-R_x/\xi_{k_x}} e^{-R_y/\xi_{k_y}}, \quad (9)$$

which is a measure of the overlap of the Wannier function centered at \mathbf{R} with that centered at the origin, sandwiched by the operator $(\mathbf{R} \times \mathbf{r})_z$. Note that the correlation function is a gauge-invariant observable because it is obtained upon integrating the gauge-invariant curvature function over a closed surface.

We can see that the correlation function $\tilde{F}_{2D}(\mathbf{R})$ decays exponentially with characteristic length scales ξ_i , indicating that ξ_i acquire the meaning of correlation lengths of the TPT with the associated critical exponents ν_i . Furthermore, the integration of the correlation function over real space yields $\int \tilde{F}_{2D}(\mathbf{R}) d^2R = F(\mathbf{k}_0, \mathbf{M})$. The curvature function at the HSP $F(\mathbf{k}_0, \mathbf{M})$ can be therefore interpreted as the analog of the susceptibility in the Landau paradigm for phase transitions [31]. For this reason, we assign to it the exponent γ that characterizes its criticality. Consequently, different values of $\{\nu_i, \gamma\}$ signify different universality classes.

We now analyze the criticality of the different TPTs that exist in this model, including transitions to phases with AEMs. We emphasize that the defining characteristic of the TPTs is its universality class, i.e., its scaling behavior, and not necessarily the magnitude of the change in the topological invariant. We apply the CRG method to the stroboscopic curvature function Eq. (6) at the representative HSPs $\mathbf{k}_0 = (0, 0)$, $(0, \pi)$ [57] to extract the criticality of the topological phase boundaries. First, via a straightforward analysis of the CRG equations, all

phase boundaries, including those delineating AEM phases, are correctly captured by the RG flow [see Figs. 1(a) and 1(b)]. Note that this approach requires very little computational effort compared to the evaluation of the time-integrated topological invariant, since solving Eq. (7) only requires us to calculate $F(\mathbf{k}, \mathbf{M})$ at a few momentum points. The fixed lines, on the other hand, illustrate the regions where the correlation length is shortest, indicating relatively localized Wannier states.

In the gapped phases, an important issue concerns the true topological invariant and the corresponding nature of the edge state. A stroboscopic approach like the ones presented here cannot address this question directly. Nonetheless, the approach does track the number of edge modes localized at 0 and π quasienergies, see Fig. 1(b). It also describes the localization lengths of these modes close to criticality via the Wannier state correlation length and its critical exponent. Deep into the gapped phase, these are such that the larger the gap, the shorter the decay length of the edge state. In the following, we focus exclusively on the critical lines and detail the two dramatically different critical behaviors uncovered in this system.

IV. QUANTUM CRITICALITY OF THE TPT AND LOW-ENERGY THEORIES

Following the stroboscopic approach outlined in the previous paragraphs, we now elaborate on the structure of the low-energy theory of the TPTs. We begin by explicitly looking at the form of the stroboscopic effective Hamiltonian and the curvature function given by Eqs. (5) and (6). The stroboscopic quasienergy dispersion $\theta(\mathbf{k})$ corresponding to the effective Hamiltonian fulfills the eigenvalue equation [13]

$$h_{\text{eff}}(\mathbf{k})\psi(\mathbf{k}) = \frac{\theta_{\mathbf{k}}}{T}\psi(\mathbf{k}) \quad (10)$$

or, equivalently,

$$U_{\mathbf{k}}(T, 0)\psi(\mathbf{k}) = e^{-i\theta_{\mathbf{k}}}\psi(\mathbf{k}). \quad (11)$$

Hence, $\theta(\mathbf{k})$ can be derived, by calculating the eigenvalues of the Floquet operator and exploiting the identity, $\arccos(z) = -i \log(z + \sqrt{z^2 - 1})$, to be

$$\theta(\mathbf{k}) = -i \log \lambda_+ = \arccos \left[\frac{\text{Tr} U_{\mathbf{k}}(T, 0)}{2} \right]. \quad (12)$$

The behavior of $\theta(\mathbf{k})$ at criticality can be used to shed light on the type of TPT taking place there. Typically, the order of the gap closure is associated to the type of low-energy theory.

For the four different transition lines in the phase diagram of the Floquet system analyzed, we show in Fig. 3 contour plots of the quasienergy dispersion that illustrate the location of the gap closures. Additionally, in Fig. 4 we also present one-dimensional cuts that depict the form of the gap closures: We can appreciate that the TPTs at $\tilde{J} = \frac{1}{3}(n - J)$ are all characterized by linear gap closures, while the one at $\tilde{J} = J$ corresponds instead to a quadratic gap closure. This visual finding was also verified through a numerical fit of the quasienergy dispersion.

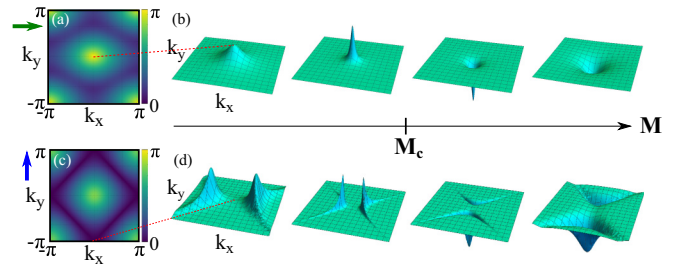


FIG. 2. Illustration of different TPTs (indicated by the arrows in Fig. 1) in the FCI as a function of tuning parameter $\mathbf{M} = J$ (b) or $\mathbf{M} = \tilde{J}$ (d). (a) Quasienergy dispersion exhibiting Dirac-cones with linear gap closure at quasienergy π for $\tilde{J} = \frac{1}{3}(n - J)$. (b) Behavior of the Berry curvature across the TPT with linear gap closure (Lorentzians). (c) Quasienergy dispersion with quadratic gap closure at quasienergy 0 for $\tilde{J} = J$. (d) Behavior of the Berry curvature across the TPT with quadratic gap closures, where non-Lorentzian pairs of peaks flip sign and change direction.

A. Floquet-Dirac criticality

Close to the $\tilde{J}_c = \frac{1}{3}(n - J)$ [e.g., green arrow in Fig. 1(b)] transitions, a Dirac-like linear gap closure at the Floquet band edge takes place at one of the HSPs $(k_x, k_y) = (0, 0)$ and $(k_x, k_y) = (\pm\pi, \pm\pi)$, and the curvature function near the HSP has the shape of a single Lorentzian peak. As $\tilde{J} \rightarrow \tilde{J}_c$, the Lorentzian peak diverges and flips signs across the transition, with critical exponents $\nu_x = \nu_y = 1$, $\gamma = 2$, fulfilling the scaling law $2 = \gamma = \nu_x + \nu_y$ (up to numerical accuracy). This result implies that these TPTs belong to the same universality class of a static 2D isotropic Dirac model [58] and this critical behavior is independent of whether in the underlying phase AEMs exist or not.

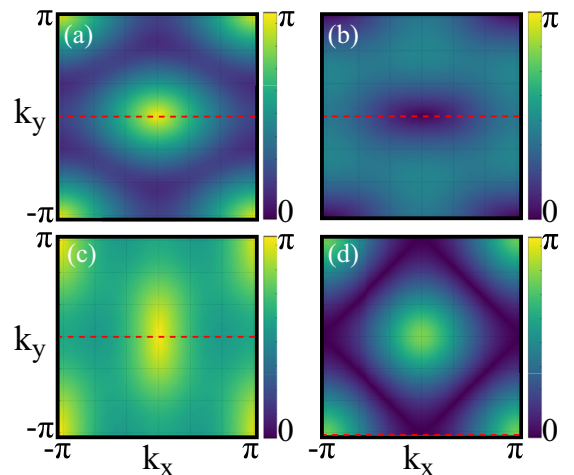


FIG. 3. Illustration of the gap closures of the quasienergy dispersion $\theta(\mathbf{k})$ at (a) $J = 0.1[4\pi]$, $\tilde{J} = 0.3[4\pi]$, (b) $J = 0.2[4\pi]$, $\tilde{J} = 0.6[4\pi]$, (c) $J = 0.3[4\pi]$, $\tilde{J} = 0.9[4\pi]$, (d) $J = 0.6[4\pi]$, $\tilde{J} = 0.6[4\pi]$. The dashed red lines indicate the cuts shown in Fig. 4.

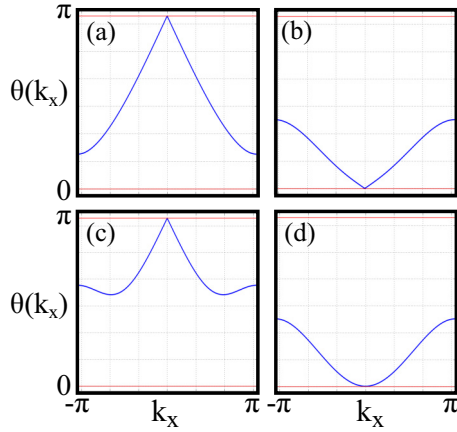


FIG. 4. Cuts of the quasienergy dispersion $\theta(k_x)$ along the k_y value of the HSPs, illustrating the kind of gap closure for each topological phase transition. The values of the energy parameters are as in Fig. 3.

B. Floquet nodal loop criticality

We now analyze the TPTs across $\tilde{J}_c = J$ [e.g., blue arrow in Fig. 1(b)], for which the gap closure is revealed to be quadratic along the nodal loops $k_y = \pm\pi \mp |k_x|$, realizing an elusive 2D NLS. For this nodal loop case, the curvature function is characterized by a pair of *non-Lorentzian* peaks symmetrically shifted away from the HSP in k_x or k_y direction (depending on the direction of the transition), as shown in Fig. 2(b). Across the TPT, the peaks simultaneously approach the HSP while diverging, flip signs, and then depart again from the HSP *but in the orthogonal direction*. For simplicity, we fix the direction of the transition such that the peaks are along the k_y direction before diverging. We note that, because of the boomerang shape of the Berry curvature along the k_x direction, the correlation length that correctly captures the conservation of the Chern number has to also be defined along the same curve, i.e., as $\xi_{\mathbf{k}_0,x} \equiv \frac{2}{FWHM(\max_{k_y}\{F(\mathbf{k})\})}$. A fit of the curvature function for this geometry reveals $\gamma = \frac{3}{2}$, $\nu_{\tilde{x}} = \frac{1}{2}$, and $\nu_y = 1$ (up to numerical accuracy). The fit is displayed in Fig. 5. These critical exponents fulfill the scaling law $\nu_{\tilde{x}} + \nu_y = \gamma$, but are distinct from Dirac models of any order of band crossing [58].

In Table I, we summarize the critical exponents and the low-energy dispersions of the two different universality classes obtained from the model. Details of fitting the critical exponents will be demonstrated in the following sections.

TABLE I. Summary of the critical exponents extracted for the two different topological phase transitions existing in the Floquet-Chern insulator, where $\tilde{\mathbf{k}}$ refers to the k coordinates around the HSPs where the corresponding gap closes.

TPT	dispersion	γ	ν_x or $\nu_{\tilde{x}}$	ν_y
$\tilde{J} = \frac{1}{3}(n - J)$	$E \propto \sqrt{\tilde{\mathbf{k}}^2 + M^2}$	2	1	1
$\tilde{J} = J$	$E \propto \sqrt{(\tilde{k}_x^2 - \tilde{k}_y^2) + M^2}$	$\frac{3}{2}$	$\frac{1}{2}$	1

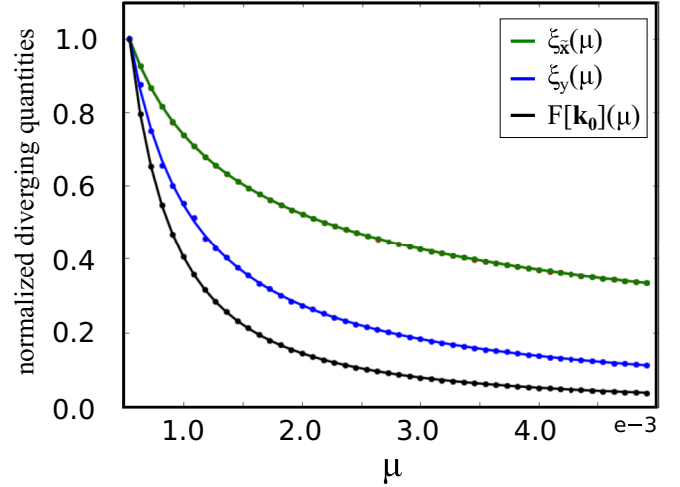


FIG. 5. Power law fit (solid lines) of the diverging quantities in the nodal loop semimetal extracted from the normalized Berry curvature. The fitted data is indicated by the dots.

This different behavior clearly indicates that the TPT at $\tilde{J}_c = J$ belongs to a different universality class than the $\tilde{J}_c = \frac{1}{3}(n - J)$ transitions described earlier. This is remarkable, as it is not customary for a single system to host two kinds of TPTs belonging to different universality classes. Quite surprising is also that the two TPTs, described by drastically different effective theories, connect the same phases along two different parameter paths.

We now present an effective theory for this Floquet-engineered NLS which perfectly captures this physics. First note that in the vicinity of $\tilde{J}_c = J$ transition line, the quasienergy dispersion around the HSPs $\mathbf{k}_0 = (0, \pm\pi)$, $(\pm\pi, 0)$ is well described by the following:

$$E = \pm A \sqrt{((k_x - k_{0,x})^2 - (k_y - k_{0,y})^2)^p + M^2}, \quad (13)$$

where the parameters A , p , and M are determined numerically. A fit of the quasienergy dispersion to the form of Eq. (13) is depicted in Fig. 6(a). Close to $\tilde{J}_c = J$, $p = 2$ and at the transition the mass term $M = 0$. Remarkably, along the entire

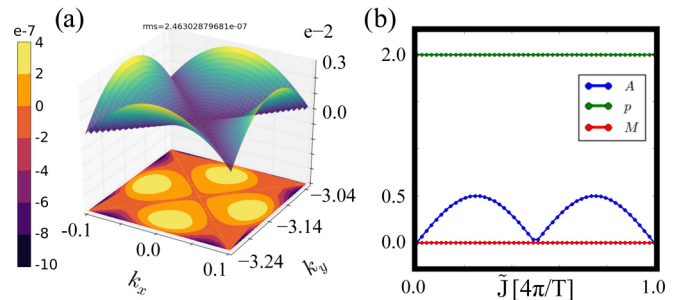


FIG. 6. (a) Two-dimensional parametric fit of the quasienergy dispersion (upper band) to Eq. (13) around the HSP $\mathbf{k}_0 = (0, -\pi)$ for the TPT at $\tilde{J} = J = 0.6$ in the FCI. The color bar on the left indicates the absolute error of the fit shown as a contour plot. (b) Dependence of the fitting parameters A , p , and M on the position of the TPT $\tilde{J} = J$, showing that only the overall scaling A changes along the transition line.

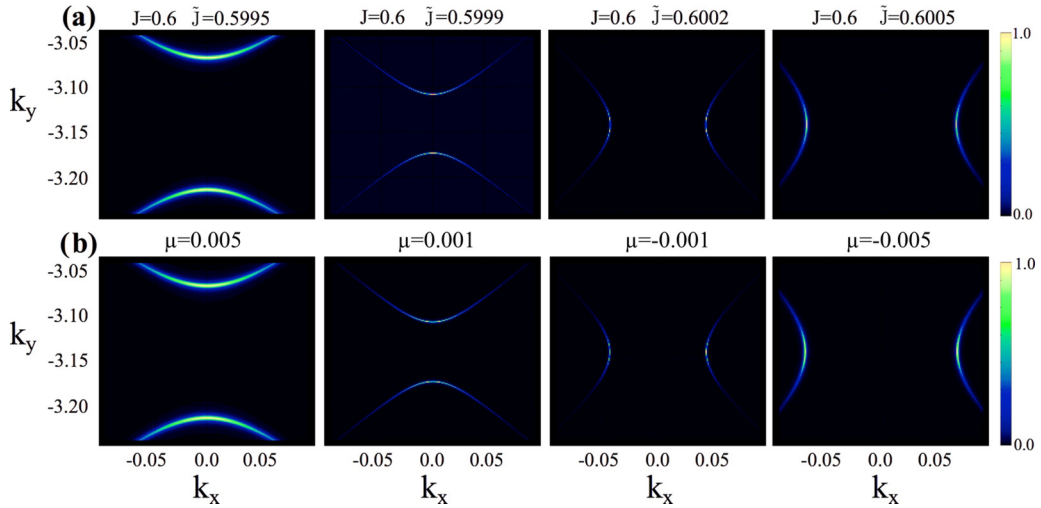


FIG. 7. (a) The normalized absolute value of the Berry curvature across the topological phase transition for the Floquet-Chern insulator (\tilde{J} in units of 4π). (b) The normalized absolute value of the Berry curvature across the topological phase transition for the nodal loop semimetal as a function of μ , with $\nu = \beta = 1.0$ and $\alpha = -1.0$.

transition line $\tilde{J}_c = J$, the dispersion exhibits the same shape with the same values of p and M (except at the multicritical point where the dispersion is identically zero), and only its overall scaling factor A varies as illustrated in Fig. 6(b). Note that A has no influence on the topology because it does not affect the gap closures.

The peculiar non-Dirac quadratic gap closure of Eq. (13) can be naturally generated along the entire $\tilde{J} = J$ transition line from a *single* 2×2 NLS Hamiltonian,

$$\begin{aligned} H_{\text{NL}} &= X(k_x, k_y)\sigma^x + Y(k_x, k_y)\sigma^y + Z(k_x, k_y)\sigma^z \quad (14) \\ &= (\mu - 2\eta(\cos k_x + \cos k_y))^2\sigma^x \\ &\quad + \alpha(\sin k_x - \sin k_y)(\cos k_x + \cos k_y)\sigma^y \\ &\quad + \beta(\sin k_x + \sin k_y)(\cos k_x + \cos k_y)\sigma^z, \quad (15) \end{aligned}$$

where σ^i are the Pauli matrices, α , β , m , μ , and η are parameters. For $\mu = 0$ (and arbitrary values of the other parameters) the energy dispersion of Eq. (15) in the vicinity of the HSPs exactly recovers Eq. (13), with the overall scale $A = \eta$ and $M = 0$. This model can further reproduce all the features observed in the FCI along the $\tilde{J} = J$ transition, including the shape of the Berry curvature across the TPT, the value of the critical exponents, and symmetries. In particular, a comparison of the two Berry curvatures across the TPTs ($J = \tilde{J} = 0.6$ for the FCI and, correspondingly, $\lambda_1 \simeq \lambda_2 = \mu$ for the NLS) is shown in Fig. 7 and reveals an excellent agreement between the two systems, indicating that the low-energy theory of the TPT in the FCI is in fact a NLS.

Surprisingly, Floquet driving realizes an extension of the model discussed in Refs. [39,40] in the context of the spin quantum Hall phases. Though 3D NLS have been abundantly discussed in the literature [59–66], physical realizations of 2D NLS (proposed as excellent candidates for spintronics) remain elusive [67–69]. Recently proposed candidate systems include interpenetrating kagome-honeycomb lattices [70] and ferromagnetic monochalcogenide monolayers [69]. Here, we see that via a simple driving protocol on a square lattice, the

resulting Floquet-engineered Hamiltonian perfectly realizes the full static model of a 2D NLS.

C. Emergent chiral mirror symmetry

The existence of two different universality classes in a simple noninteracting model indicates that they must be related to different symmetries. In fact, the effective nodal loop theory is characterized by an increased chiral mirror symmetry that can be traced back to the driving scheme. We have numerically verified that the Floquet effective Hamiltonian fulfills the following symmetry operations:

$$\mathcal{C}h_{\text{eff}}(k_x, k_y)\mathcal{C}^{-1} = -h_{\text{eff}}(-k_x, -k_y), \quad (16)$$

$$\mathcal{I}h_{\text{eff}}(k_x, k_y)\mathcal{I}^{-1} = h_{\text{eff}}(-k_x, -k_y), \quad (17)$$

$$\mathcal{D}h_{\text{eff}}(k_x, k_y)\mathcal{D}^{-1} = h_{\text{eff}}(k_x \pm \pi, k_y \pm \pi), \quad (18)$$

with $\mathcal{C} = \sigma^z \circ \mathcal{K}$, $\mathcal{I} = \sigma^x$, and $\mathcal{D} = \sigma^z$. These symmetries are charge conjugation, inversion, and displacement by $\pm\pi$ (reduction of the Brillouin zone to half), respectively.

Additionally, at $\tilde{J} = J$ corresponding to the nodal loop low-energy theory, a driving-induced new symmetry emerges,

$$\tilde{\mathcal{M}}h_{\text{eff}}(k_x, k_y)\tilde{\mathcal{M}}^{-1} = -h_{\text{eff}}(k_y, k_x), \quad (19)$$

with $\tilde{\mathcal{M}} = \sigma^y$. We term this symmetry chiral mirror symmetry, as it can be decomposed into a combination of a mirror symmetry \mathcal{M} and chiral or sublattice symmetry \mathcal{S} . We note, however, that the two separate symmetry operations \mathcal{M} and \mathcal{S} need not be fulfilled when chiral mirror symmetry is present, much like a chiral symmetry can exist on its own even when time-reversal and charge-conjugation symmetries are not separately fulfilled [46]. In fact, we empirically verified that the effective Floquet Hamiltonian does not have separate mirror and chiral symmetries.

The combination of charge conjugation and chiral mirror symmetry protects the nodal loop Hamiltonian Eq. (15) from mass terms. Chiral mirror symmetry implies $Y(k_x, k_y) = -Y(k_y, k_x)$, which forbids mass terms in σ^y . Charge

conjugation instead implies $Z(k_x, k_y) = -Z(-k_x, -k_y)$, which forbids mass terms in σ^z . The parameter μ controls the gap closure, such that the nodal loop sits at zero (quasi)energy when $\mu = 0$ (and, correspondingly, $\tilde{J} = J$ for the FCI).

The chiral mirror symmetry is a direct consequence of the driving scheme applied to the Chern insulator and can be reformulated as a property of the Floquet operator $U(\mathbf{k}, T)$:

$$\begin{aligned} \bar{\mathcal{M}}h_{\text{eff}}(k_x, k_y)\bar{\mathcal{M}}^{-1} &= -h_{\text{eff}}(k_y, k_x) \\ \iff h_{\text{eff}}^*(k_x, k_y) &= h_{\text{eff}}(k_y, k_x) \\ \iff U(k_x, k_y; T) &= U^\top(k_y, k_x; T), \end{aligned} \quad (20)$$

where \top denotes matrix transposition. This property can be generalized to other forms of mirror symmetries, such as reflections with respect to a different axis ($k_x \leftrightarrow k_y$ is a reflection with respect to $\hat{a} = \frac{1}{\sqrt{2}}(1, 1)$ in \mathbf{k} space). The general condition to have chiral mirror symmetry in the effective theory of the Floquet Hamiltonian is then

$$U(\mathbf{k}, T) = U^\top(\mathbf{k}^{\mathcal{M}}, T), \quad (21)$$

where $\mathbf{k}^{\mathcal{M}}$ are the k coordinates transformed under the chiral mirror symmetry. By Floquet engineering the stroboscopic time evolution to have such a property, it is in principle possible to generate a whole hierarchy of effective Floquet Hamiltonians with chiral mirror symmetry that can stabilize NLS phases.

D. Multicritical points

Lastly, we consider the three multicritical points shown in the phase diagram. Because the two kinds of TPTs of the model occur at different HSPs, the points at $\tilde{J} = J = \pi/T, 3\pi/T$ are found to exhibit both a peak divergence at $\mathbf{k}_0 = (0, 0)$ and $\mathbf{k}_0 = (\pm\pi, \pm\pi)$ (linear gap closure at quasienergy π), and a double-peak divergence around $\mathbf{k}_0 = (0, \pm\pi)$ and $\mathbf{k}_0 = (\pm\pi, 0)$ (quadratic gap closure at quasienergy 0). These multicritical points therefore display a coexistence of both TPTs belonging to different universality classes. The points at $\tilde{J} = J = 2\pi n/T, n \in [0, 1, 2]$ are instead not critical, because there the Floquet operator $U(\mathbf{k}, T) = e^{ih_{\text{eff}}(\mathbf{k})T}$ is precisely the identity and the quasienergy dispersion $h_{\text{eff}}(\mathbf{k})T$ collapses to a flat band at 0. This behavior at $\tilde{J} = J = 2\pi/T$ is also detected in the CRG flow, where fixed lines and critical lines meet. The loss of criticality around these points is further corroborated by the fit of the quasienergy dispersion (Fig. 6), which highlights the flat band as $A \rightarrow 0$. Such multicriticality in static topological systems has not been widely explored. To our knowledge, the only two examples of static free fermion models exhibiting multicriticality of TPTs are an extended Su-Schrieffer-Heeger model in the presence of a synthetic potential [35], and a one-dimensional topological band insulator with spin-orbit coupling [71]. This indicates that in static systems a certain degree of engineering beyond usual linear Dirac models is required to generate multicriticality. In contrast, our paper shows that multicriticality can be easily realized in simple periodically driven systems by making use of the additional gap-closure channel at quasienergy π provided by the time periodicity.

E. Experimental realization and detection

The multiple universality classes and the multicriticality uncovered in the present paper can be experimentally detected in photonic and cold-atomic realizations of the model. The AEMs existing in this model have already been experimentally probed in photonic systems with state recycling [37,41]. Here, the measurement of the Berry curvature needed to extract the critical exponents could be performed from measurements of the anomalous displacement of wave packets under optical pulse pumping in coupled fiber loops, similar to what was highlighted in Ref. [72]. Another possible realization of the model is with ultracold atoms placed in a square optical lattice, where the modulations of the hopping between neighboring sites can be induced by a time-dependent superlattice [73]. In this setup, the measurement of the Berry curvature can be achieved through quantum interference maps of the Berry curvature [74] or force-induced wave-packet velocity measurements [75,76].

V. CONCLUSIONS AND OUTLOOK

In summary, we demonstrate how to generate quantum multicriticality and exotic 2D nodal loops by a simple periodic driving in an otherwise ordinary topological insulator. Through applying the CRG method to the Berry curvature, we have delineated the entire topological phase diagram regardless of the details of the system. The extracted critical exponents indicate that the system hosts TPTs belonging to two different universality classes, namely, a Dirac low-energy theory with linear gap closures, and a NLS low-energy theory with quadratic gap closures. Remarkably, these different universality classes can coexist at certain discrete points, revealing an unprecedented phenomenon of topological multicriticality in 2D. The nodal loop TPTs were also shown to result from a driving-induced additional chiral mirror symmetry, which is absent for the Dirac-type TPTs and helps stabilize the band inversion from certain perturbing mass terms. Our paper thus paves the path for future explorations and realizations of complex topological states of matter by engineering emergent symmetries in simple systems using judiciously chosen Floquet driving protocols.

Despite the enhanced symmetry provided by the driving procedure, the nodal loops of this particular Floquet model are not fully topologically protected, because mass terms along x are still allowed to shift the band inversion away from zero quasienergy. It is, however, feasible to expect that similar emerging symmetries in different models could give rise to a fully symmetry-protected NLS phase, for instance, if the driving realizes a time-reversal symmetry $\mathcal{T} = \sigma^y \circ \mathcal{K}$. This point is therefore worth investigating in future work.

Another question opened up by our study is the stability of the nodal loops with respect to interactions. Possibly, the nodal loops in the driven system are unstable to interactions like Weyl and NLSs in three dimensions [77]. Additionally, interactions can introduce various orderings like ferromagnetic, antiferromagnetic, and charge-density wave ordering in the bulk, which could be detrimental for topological states [78]. Interactions also raise the specter of drive-induced heating.

Typically, integrable systems such as free-fermion systems are not expected to thermalize to a trivial Gibbs ensemble. Exceptions are the recently studied free fermion systems with specific disorder and quasiperiodic potentials, which were shown to exhibit heating to a high-temperature state [79]. Even in these cases, the amount of energy absorption was shown to be directly proportional to the driving period T , and remains low for small periods. We therefore expect our results to be stable to potential sources of heating like weak disorder for experimentally relevant timescales [80]. Furthermore, even in systems which are expected to heat up, sufficiently long prethermalization regimes are often found, permitting the

exploration of the new physics triggered by driving [81]. A detailed study of the impact of interactions in the Floquet case and the associated problem of heating is beyond the scope of the present paper and is left for future studies.

ACKNOWLEDGMENTS

We kindly acknowledge financial support by G. Anderhuggen and the ETH Zürich Foundation, and the productivity in research fellowship from CNPq. The authors would like to thank A. Schnyder, M. Rudner, and T. Bzdušek for fruitful discussions.

-
- [1] T. Kitagawa, E. Berg, M. Rudner, and E. Demler, *Phys. Rev. B* **82**, 235114 (2010).
- [2] N. H. Lindner, G. Refael, and V. Galitski, *Nat. Phys.* **7**, 490 (2011).
- [3] J. Cayssol, B. Dóra, F. Simon, and R. Moessner, *Phys. Status Solidi RRL* **7**, 101 (2013).
- [4] F. Harper and R. Roy, *Phys. Rev. Lett.* **118**, 115301 (2017).
- [5] R. Roy and F. Harper, *Phys. Rev. B* **96**, 155118 (2017).
- [6] I. Esin, M. S. Rudner, G. Refael, and N. H. Lindner, *Phys. Rev. B* **97**, 245401 (2018).
- [7] D. E. Liu, A. Levchenko, and H. U. Baranger, *Phys. Rev. Lett.* **111**, 047002 (2013).
- [8] M. Thakurathi, A. A. Patel, D. Sen, and A. Dutta, *Phys. Rev. B* **88**, 155133 (2013).
- [9] M. Thakurathi, K. Sengupta, and D. Sen, *Phys. Rev. B* **89**, 235434 (2014).
- [10] P. Wang, Q.-F. Sun, and X. C. Xie, *Phys. Rev. B* **90**, 155407 (2014).
- [11] P. D. Sacramento, *Phys. Rev. B* **91**, 214518 (2015).
- [12] M. Thakurathi, D. Loss, and J. Klinovaja, *Phys. Rev. B* **95**, 155407 (2017).
- [13] P. Mollignini, E. van Nieuwenburg, and R. Chitra, *Phys. Rev. B* **96**, 125144 (2017).
- [14] P. Mollignini, W. Chen, and R. Chitra, *Phys. Rev. B* **98**, 125129 (2018).
- [15] T. Cadez, R. Mondaini, and P. D. Sacramento, *Phys. Rev. B* **99**, 014301 (2019).
- [16] R. W. Bomantara, G. N. Raghava, L. Zhou, and J. Gong, *Phys. Rev. E* **93**, 022209 (2016).
- [17] L. Zhou, C. Chen, and J. Gong, *Phys. Rev. B* **94**, 075443 (2016).
- [18] R. W. Bomantara and J. Gong, *Phys. Rev. B* **94**, 235447 (2016).
- [19] L. Bucciattini, S. Roy, S. Kitamura, and T. Oka, *Phys. Rev. B* **96**, 041126(R) (2017).
- [20] H. Hübener, M. A. Sentef, U. D. Giovannini, A. F. Kemper, and A. Rubio, *Nat. Commun.* **8**, 13940 (2017).
- [21] J. Cao, F. Qi, and Y. Xiang, *Europhys. Lett.* **119**, 57008 (2017).
- [22] L. Li, S. Chesi, C. Yin, and S. Chen, *Phys. Rev. B* **96**, 081116(R) (2017).
- [23] R. Chen, B. Zhou, and D.-H. Xu, *Phys. Rev. B* **97**, 155152 (2018).
- [24] L. Li, C. H. Lee, and J. Gong, *Phys. Rev. Lett.* **121**, 036401 (2018).
- [25] M. Fisher, in *Multicriticality: A Theoretical Introduction, in Multicritical Phenomena*, edited by R. Pynn and A. Skjeltorp (Springer, Boston, MA, 1984).
- [26] M. Zacharias, P. Wölfle, and M. Garst, *Phys. Rev. B* **80**, 165116 (2009).
- [27] L. Carr, *Understanding Quantum Phase Transitions*, Condensed Matter Physics (CRC Press, Boca Raton, FL, 2010).
- [28] J. H. Pixley, A. Shashi, and A. H. Nevidomskyy, *Phys. Rev. B* **90**, 214426 (2014).
- [29] M. Brando, A. Kerkau, A. Todorova, Y. Yamada, P. Khuntia, T. Förster, U. Burkhard, M. Baenitz, and G. Kreiner, *J. Phys. Soc. Jpn.* **85**, 084707 (2016).
- [30] W. Chen, *J. Phys.: Condens. Matter* **28**, 055601 (2016).
- [31] W. Chen, M. Sigrist, and A. P. Schnyder, *J. Phys.: Condens. Matter* **28**, 365501 (2016).
- [32] S. Kourtis, T. Neupert, C. Mudry, M. Sigrist, and W. Chen, *Phys. Rev. B* **96**, 205117 (2017).
- [33] W. Chen, *Phys. Rev. B* **97**, 115130 (2018).
- [34] P. Mollignini, R. Chitra, and W. Chen, *Europhys. Lett.* **128**, 36001 (2019).
- [35] S. Rufo, N. Lopes, M. A. Continentino, and M. A. R. Griffith, *Phys. Rev. B* **100**, 195432 (2019).
- [36] M. S. Rudner, N. H. Lindner, E. Berg, and M. Levin, *Phys. Rev. X* **3**, 031005 (2013).
- [37] S. Mukherjee, A. Spracklen, M. Valiente, E. Andersson, P. Öhberg, N. Goldman, and R. R. Thomson, *Nat. Commun.* **8**, 13918 (2017).
- [38] S. Yao, Z. Yan, and Z. Wang, *Phys. Rev. B* **96**, 195303 (2017).
- [39] X.-L. Qi, Y.-S. Wu, and S.-C. Zhang, *Phys. Rev. B* **74**, 085308 (2006).
- [40] L. Li and M. A. N. Araújo, *Phys. Rev. B* **94**, 165117 (2016).
- [41] S. Mukherjee, H. K. Chandrasekharan, P. Öhberg, N. Goldman, and R. R. Thomson, *Nat. Commun.* **9**, 4209 (2018).
- [42] T. Dittrich, P. Hänggi, G.-L. Ingold, B. Kramer, G. Schön, and W. Zwerger, *Quantum Transport and Dissipation* (Wiley-VCH, Weinheim, Germany, 1998).
- [43] F. N. Ünal, B. Seradjeh, and A. Eckardt, *Phys. Rev. Lett.* **122**, 253601 (2019).
- [44] F. N. Ünal, A. Eckardt, and R.-J. Slager, *Phys. Rev. Research* **1**, 022003(R) (2019).
- [45] R. Bott and R. Seeley, *Commun. Math. Phys.* **62**, 235 (1978).
- [46] C.-K. Chiu, J. C. Y. Teo, A. P. Schnyder, and S. Ryu, *Rev. Mod. Phys.* **88**, 035005 (2016).
- [47] W. Chen, M. Legner, A. Rüegg, and M. Sigrist, *Phys. Rev. B* **95**, 075116 (2017).
- [48] W. Chen and M. Sigrist, Topological phase transitions: Criticality, universality, and renormalization group approach, in *Advanced Topological Insulators* (Wiley-Scrivener, Beverly, MA, 2019).

- [49] X. Wang, J. R. Yates, I. Souza, and D. Vanderbilt, *Phys. Rev. B* **74**, 195118 (2006).
- [50] N. Marzari, A. A. Mosto, J. R. Yates, I. Souza, and D. Vanderbilt, *Rev. Mod. Phys.* **84**, 1419 (2012).
- [51] M. Gradhand, D. V. Fedorov, F. Pientka, P. Zahn, I. Mertig, and B. L. Györfy, *J. Phys. Condens. Matter* **24**, 213202 (2012).
- [52] T. Thonhauser, D. Ceresoli, D. Vanderbilt, and R. Resta, *Phys. Rev. Lett.* **95**, 137205 (2005).
- [53] D. Xiao, J. Shi, and Q. Niu, *Phys. Rev. Lett.* **95**, 137204 (2005).
- [54] D. Ceresoli, T. Thonhauser, D. Vanderbilt, and R. Resta, *Phys. Rev. B* **74**, 024408 (2006).
- [55] J. Shi, G. Vignale, D. Xiao, and Q. Niu, *Phys. Rev. Lett.* **99**, 197202 (2007).
- [56] I. Souza and D. Vanderbilt, *Phys. Rev. B* **77**, 054438 (2008).
- [57] Because of the C_4 symmetry of the lattice, all other HSPs (e.g., $\mathbf{k}_0 = (\pi, \pi)$, $(\pi, 0)$, etc.) are obtained by a shift with the reciprocal vectors $\mathbf{b}_1 = (\pi, \pi)$ and/or $\mathbf{b}_2 = (-\pi, \pi)$ and yield the same results as the two different representative HSPs $\mathbf{k}_0 = (0, 0)$, $(0, \pi)$.
- [58] W. Chen and A. P. Schnyder, *New J. Phys.* **21**, 073003 (2019).
- [59] K. Mullen, B. Uchoa, and D. T. Glatzhofer, *Phys. Rev. Lett.* **115**, 026403 (2015).
- [60] J.-W. Rhim and Y. B. Kim, *Phys. Rev. B* **92**, 045126 (2015).
- [61] L.-K. Lim and R. Moessner, *Phys. Rev. Lett.* **118**, 016401 (2017).
- [62] N. B. Kopnin, T. T. Heikkilä, and G. E. Volovik, *Phys. Rev. B* **83**, 220503(R) (2011).
- [63] R. Li, H. Ma, X. Cheng, S. Wang, D. Li, Z. Zhang, Y. Li, and X.-Q. Chen, *Phys. Rev. Lett.* **117**, 096401 (2016).
- [64] Y.-H. Chan, C.-K. Chiu, M. Y. Chou, and A. P. Schnyder, *Phys. Rev. B* **93**, 205132 (2016).
- [65] Y. Wang and R. M. Nandkishore, *Phys. Rev. B* **95**, 060506(R) (2017).
- [66] J. Liu and L. Balents, *Phys. Rev. B* **95**, 075426 (2017).
- [67] A. A. Burkov, M. D. Hook, and L. Balents, *Phys. Rev. B* **84**, 235126 (2011).
- [68] R. Yu, Z. Fang, X. Dai, and H. Weng, *Front. Phys.* **12**, 127202 (2017).
- [69] X. Zhou, R.-W. Zhang, Z. Zhang, D.-S. Ma, W. Feng, Y. Mokrousov, and Y. Yao, *J. Phys. Chem. Lett.* **10**, 3101 (2019).
- [70] J. L. Lu, W. Luo, X. Y. Li, S. Q. Yang, J. X. Cao, X. G. Gong, and H. J. Xiang, *Chin. Phys. Lett.* **34**, 057302 (2017).
- [71] M. Malard, D. Brandao, P. Eduardo de Brito, and H. Johannesson, *arXiv:2001.10079*.
- [72] M. Wimmer, H. M. Price, I. Carusotto, and U. Peschel, *Nat. Phys.* **13**, 545 (2017).
- [73] M. D. Reichl and E. J. Mueller, *Phys. Rev. A* **89**, 063628 (2014).
- [74] L. Duca, T. Li, M. Reitter, I. Bloch, M. Schleier-Smith, and U. Schneider, *Science* **347**, 288 (2015).
- [75] H. M. Price and N. R. Cooper, *Phys. Rev. A* **85**, 033620 (2012).
- [76] G. Jotzu, M. Messer, R. Desbuquois, M. Lebrat, T. Uehlinger, D. Greif, and T. Esslinger, *Nature* **515**, 237 (2014).
- [77] J. Kang, J. Zou, K. Li, S.-L. Yu, and L.-B. Shao, *Sci. Rep.* **9**, 2824 (2019).
- [78] B. Roy, *Phys. Rev. B* **96**, 041113(R) (2017).
- [79] T. Ishii, T. Kuwahara, T. Mori, and N. Hatano, *Phys. Rev. Lett.* **120**, 220602 (2018).
- [80] J. Choi, H. Zhou, S. Choi, R. Landig, W. W. Ho, J. Isoya, F. Jelezko, S. Onoda, H. Sumiya, D. A. Abanin *et al.*, *Phys. Rev. Lett.* **122**, 043603 (2019).
- [81] K. Singh, C. J. Fujiwara, Z. A. Geiger, E. Q. Simmons, M. Lipatov, A. Cao, P. Dotti, S. V. Rajagopal, R. Senaratne, T. Shimasaki *et al.*, *Phys. Rev. X* **9**, 041021 (2019).